

# Adaptive Deep Learning for High-Dimensional Hamilton-Jacobi-Bellman Equations

Tenavi Nakamura-Zimmerer<sup>1</sup>    Qi Gong<sup>2</sup>    Wei Kang<sup>3</sup>

September 24, 2019

## Abstract

Computing optimal feedback controls for nonlinear systems generally requires solving Hamilton-Jacobi-Bellman (HJB) equations, which are notoriously difficult when the state dimension is large. Existing strategies for high-dimensional problems generally rely on specific, restrictive problem structures, or are valid only locally around some nominal trajectory. In this paper, we propose a data-driven method to approximate semi-global solutions to HJB equations for general high-dimensional nonlinear systems and compute optimal feedback controls in real-time. To accomplish this, we model solutions to HJB equations with neural networks (NNs) trained on data generated without discretizing the state space. Training is made more effective and data-efficient by leveraging the known physics of the problem and using the partially-trained NN to aid in adaptive data generation. We demonstrate the effectiveness of our method by learning solutions to HJB equations corresponding to the attitude control of a six-dimensional nonlinear rigid body, and nonlinear systems of dimension up to 30 arising from the stabilization of a Burgers'-type partial differential equation. The trained NNs are then used for real-time optimal feedback control of these systems.

## 1 Introduction

For the optimal control of nonlinear dynamical systems, it is well-known that open-loop controls are not robust to model uncertainty or disturbances. For slowly evolving processes, it is possible to use model predictive control by recomputing the open-loop optimal solution for a relatively short time horizon in the future. However, for most applications one typically desires an optimal feedback control law, as feedback controls are inherently more robust to disturbances. Using dynamic programming, the optimal feedback control is computed

---

<sup>1</sup>Department of Applied Mathematics, Baskin School of Engineering, University of California, Santa Cruz (tenakamu@ucsc.edu).

<sup>2</sup>Professor, Department of Applied Mathematics, Baskin School of Engineering, University of California, Santa Cruz.

<sup>3</sup>Professor, Department of Applied Mathematics, Naval Postgraduate School, Monterey, CA.

by solving a (discretized) Hamilton-Jacobi-Bellman (HJB) equation, a partial differential equation (PDE) in  $n$  spatial dimensions plus time. The size of the discretized problem increases exponentially with  $n$ , making direct solution intractable for even moderately large problems. This is the so-called “curse of dimensionality.”

For this reason, there is an extensive literature on methods of finding approximate solutions for HJB equations. We have no intention to give a full review of existing results except for a short list of some related publications, [2, 25, 8, 26, 3, 12, 10, 18, 19, 21, 30, 16, 13, 29]. These existing methods suffer one or more of the following drawbacks: the problem’s dimension is limited; the accuracy of the solution is hard to verify for general systems; the solution may be valid only in a small neighborhood of a point; or the system model must have certain special algebraic structure.

In [20, 21], semi-global solutions to HJB equations are computed by constructing a sparse discretization of the state space, then solving a two-point boundary value problem (BVP) at each point on the grid. The BVP is *causality-free*, i.e. each problem can be computed independently. Causality-free algorithms have been used to solve various types of PDEs, such as conservation laws [22], HJ and HJB equations [32, 9], and semilinear parabolic PDEs [13]. The causality-free property is achieved by means of Hopf formula and convex optimization in [9], backward stochastic differential equations in [13], and Pontryagin’s minimum principle in [21]. Causality-free algorithms are attractive because the computation does not depend on a grid, and hence can be applied to high-dimensional problems. Some causality-free methods are too slow for online computation, but they are perfectly parallelizable so can be used to generate large data sets offline. Such data sets can then be used to construct faster solutions such as sparse grid interpolation [20, 21] or, as in this paper, neural networks.

Using neural networks (NNs) as a basis for solving HJB equations is not by itself a new idea, and recent deep learning approaches have produced promising results; see for instance [30, 29, 13, 27, 15]. To the best of our knowledge, contemporary NN-based techniques generally rely on either minimizing the residual of the PDE and (artificial) boundary conditions at randomly sampled collocation points [30, 29]; discretizing the time domain and solving stochastic differential equations with a NN basis [13, 27]; or, due to computational limitations, modeling the solution and its gradient in a small neighborhood of a nominal trajectory [15].

In this paper, we develop a computational method for solving high-dimensional HJB equations and generating fully nonlinear optimal feedback controls. Our approach is data-driven and consists of three main steps. In the first step, a small set of open-loop optimal control solutions is generated using a causality-free algorithm, which is based on a BVP derived from Pontryagin’s minimum principle. In the second step, we use the data set to train a NN to approximate the solution to the HJB equation, called the *value function*, and its gradient. Supplying this gradient information encourages the NN to learn the shape of the value function, rather than just fitting point data. During training, we estimate the number of samples needed to obtain a good model. Additional samples are chosen in regions where the value function is difficult to learn, and are obtained quickly with the aid of the NN. In this sense our method involves *adaptive sampling*. Lastly, the accuracy of the NN is verified on another data set that is generated using the same causality free algorithm from the first step. Unlike other NN-based methods, our approach requires no temporal discretization, computation of expensive PDE residuals, and the solution is valid over large

spatial domains.

As an illustrative example, the method is applied to the optimal attitude control of a rigid-body satellite equipped with momentum wheels. This is a highly nonlinear problem with  $n = 6$  spatial dimensions and  $m = 3$  control inputs. With the proposed method, we obtain a model of the value function with accuracy comparable to that obtained in [21], but require far fewer sample trajectories to do so. Scalability of the method is tested on problems of dimension  $n = 10, 20,$  and  $30$  arising from pseudospectral discretization of a Burgers'-type PDE. We show that the method is capable of handling these high-dimensional problems without simplifying the dynamics.

Through these examples, we demonstrate several advantages and potential capabilities of the proposed framework. These include solving HJB equations over semi-global domains with empirically validated levels of accuracy, computationally efficient NN-based feedback control for real-time applications, and progressive generation of rich data sets. Solution of high-dimensional problems is enabled by efficient and adaptive causality-free data generation, physics-informed learning, and the inherent capacity of NNs for dealing with high-dimensional data.

## 2 A causality-free method for HJB

We consider fixed final time optimal control problems of the form

$$\begin{cases} \underset{\mathbf{u} \in \mathcal{U}}{\text{minimize}} & F(\mathbf{x}(t_f)) + \int_0^{t_f} L(t, \mathbf{x}, \mathbf{u}) dt, \\ \text{subject to} & \dot{\mathbf{x}}(t) = \mathbf{f}(t, \mathbf{x}, \mathbf{u}), \\ & \mathbf{x}(0) = \mathbf{x}_0. \end{cases} \quad (2.1)$$

Here  $\mathbf{x}(t) : [0, t_f] \rightarrow \mathcal{X} \subseteq \mathbb{R}^n$  is the state,  $\mathbf{u}(t, \mathbf{x}) : [0, t_f] \times \mathcal{X} \rightarrow \mathcal{U} \subseteq \mathbb{R}^m$  is the control,  $\mathbf{f}(t, \mathbf{x}, \mathbf{u}) : [0, t_f] \times \mathcal{X} \times \mathcal{U} \rightarrow \mathbb{R}^n$  is a Lipschitz continuous vector field,  $F(\mathbf{x}(t_f)) : \mathcal{X} \rightarrow \mathbb{R}$  is the terminal cost, and  $L(t, \mathbf{x}, \mathbf{u}) : [0, t_f] \times \mathcal{X} \times \mathcal{U} \rightarrow \mathbb{R}$  is the running cost. For simplicity let the final time  $t_f < \infty$  be fixed. For a given initial condition  $\mathbf{x}(0) = \mathbf{x}_0$ , many numerical methods exist to compute the optimal open-loop solution,

$$\mathbf{u} = \mathbf{u}^*(t; \mathbf{x}_0). \quad (2.2)$$

The open-loop control (2.2) which solves (2.1) is valid for all  $t \in [0, t_f]$ , but only for the fixed initial condition  $\mathbf{x}(0) = \mathbf{x}_0$ . Due to various sources of disturbance and real-time application requirements, for practical implementation one typically desires an optimal control in closed-loop feedback form,

$$\mathbf{u} = \mathbf{u}^*(t, \mathbf{x}), \quad (2.3)$$

which can be evaluated online given any  $t \in [0, t_f]$  and a measurement of  $\mathbf{x} \in \mathcal{X}$ .

To compute the optimal feedback control, we follow the standard procedure in dynamic programming (see e.g. [24]) and define a family of optimal control problems:

$$\begin{cases} \underset{\mathbf{u} \in \mathcal{U}}{\text{minimize}} & F(\mathbf{y}(t_f)) + \int_t^{t_f} L(\tau, \mathbf{y}, \mathbf{u}) d\tau, \\ \text{subject to} & \dot{\mathbf{y}}(\tau) = \mathbf{f}(\tau, \mathbf{y}, \mathbf{u}), \\ & \mathbf{y}(t) = \mathbf{x}. \end{cases} \quad (2.4)$$

Now we define the value function as the optimal cost-to-go of (2.4):

$$V(t, \mathbf{x}) := \inf_{\mathbf{u} \in \mathcal{U}} \left\{ F(\mathbf{y}(t_f)) + \int_t^{t_f} L(\tau, \mathbf{y}, \mathbf{u}) d\tau \right\}, \quad (2.5)$$

subject to  $\dot{\mathbf{y}}(\tau) = \mathbf{f}(\tau, \mathbf{y}, \mathbf{u})$  and  $\mathbf{y}(t) = \mathbf{x}$ . The value function is the unique (viscosity) solution to the Hamilton-Jacobi-Bellman (HJB) PDE,

$$\begin{cases} -V_t(t, \mathbf{x}) - \min_{\mathbf{u} \in \mathcal{U}} \{ L(t, \mathbf{x}, \mathbf{u}) + [V_{\mathbf{x}}(t, \mathbf{x})]^T \mathbf{f}(t, \mathbf{x}, \mathbf{u}) \} = 0, \\ V(t_f, \mathbf{x}) = F(\mathbf{x}), \end{cases} \quad (2.6)$$

where we denote  $V_t := \partial V / \partial t$  and  $V_{\mathbf{x}} := \partial V / \partial \mathbf{x}$ . This PDE provides both necessary and sufficient conditions for optimality.

For an alternative and perhaps clearer way to write (2.6), we first define the Hamiltonian

$$H(t, \mathbf{x}, \boldsymbol{\lambda}, \mathbf{u}) := L(t, \mathbf{x}, \mathbf{u}) + \boldsymbol{\lambda}^T \mathbf{f}(t, \mathbf{x}, \mathbf{u}), \quad (2.7)$$

where  $\boldsymbol{\lambda}(t) : [0, t_f] \rightarrow \mathbb{R}^n$  is the costate. The optimal control satisfies

$$\mathbf{u}^*(t, \mathbf{x}) = \mathbf{u}^*(t, \mathbf{x}; \boldsymbol{\lambda}) = \arg \min_{\mathbf{u} \in \mathcal{U}} H(t, \mathbf{x}, \boldsymbol{\lambda}, \mathbf{u}). \quad (2.8)$$

If we write  $H^*(t, \mathbf{x}, \boldsymbol{\lambda}) := H(t, \mathbf{x}, \boldsymbol{\lambda}, \mathbf{u}^*)$ , then the HJB equation (2.6) can be written as

$$\begin{cases} -V_t(t, \mathbf{x}) - H^*(t, \mathbf{x}, V_{\mathbf{x}}) = 0, \\ V(t_f, \mathbf{x}) = F(\mathbf{x}). \end{cases} \quad (2.9)$$

If (2.9) can be solved, then the optimal control is computed by substituting

$$\boldsymbol{\lambda}(t) = V_{\mathbf{x}}(t, \mathbf{x}) \quad (2.10)$$

into (2.8) to get

$$\mathbf{u}^*(t, \mathbf{x}) = \arg \min_{\mathbf{u} \in \mathcal{U}} H(t, \mathbf{x}, V_{\mathbf{x}}, \mathbf{u}). \quad (2.11)$$

This means that with  $V_{\mathbf{x}}(\cdot)$  available, the feedback control is obtained as the solution of an (ideally straightforward) optimization problem.

To make use of eq. (2.11), we need an efficient way to approximate the value function and its gradient. Like [20, 21], rather than solve the full HJB equation (2.9) on a grid, we exploit the fact that its characteristics evolve according to

$$\begin{cases} \dot{\mathbf{x}}(t) = \frac{\partial H}{\partial \boldsymbol{\lambda}} = \mathbf{f}(t, \mathbf{x}, \mathbf{u}^*(t, \mathbf{x}, \boldsymbol{\lambda})), \\ \dot{\boldsymbol{\lambda}}(t) = -\frac{\partial H}{\partial \mathbf{x}}(t, \mathbf{x}, \boldsymbol{\lambda}, \mathbf{u}^*(t, \mathbf{x}, \boldsymbol{\lambda})), \\ \dot{v}(t) = -L(t, \mathbf{x}, \mathbf{u}^*(t, \mathbf{x}, \boldsymbol{\lambda})), \end{cases} \quad (2.12)$$

with two-point split boundary conditions

$$\begin{cases} \mathbf{x}(0) = \mathbf{x}_0, \\ \boldsymbol{\lambda}(t_f) = \frac{dF}{d\mathbf{x}}(\mathbf{x}(t_f)), \\ v(t_f) = F(\mathbf{x}(t_f)). \end{cases} \quad (2.13)$$

For any given initial condition  $\mathbf{x}_0$ , the optimal control and value function along the characteristic  $\mathbf{x}(t; \mathbf{x}_0)$  are then given by

$$\mathbf{u}^*(t, \mathbf{x}) = \mathbf{u}^*(t; \mathbf{x}_0), \quad V(t, \mathbf{x}) = v(t; \mathbf{x}_0). \quad (2.14)$$

In [20, 21], the two-point BVP (2.12–2.13) is solved for each point in a sparse grid. The value function and its gradient are then calculated with high-dimensional interpolation. This technique is called the sparse grid characteristics method. However, even using a sparse grid the number of points grows like  $O(N(\log N)^{n-1})$ , where  $n$  is the state dimension and  $N$  is the number of grid points in each dimension. Thus one may have to solve a prohibitively large number of BVPs for higher-dimensional problems. Instead of sparse grid interpolation, we use data from solved BVPs to train a NN to approximate the value function  $V(t, \mathbf{x})$ . This approach is completely grid-free and hence applicable in high dimensions.

The two-point BVP (2.12–2.13) provides a necessary condition for optimality and is well-known in optimal control theory as Pontryagin’s Minimum Principle (PMP). In general, however, solutions of the BVP are not unique and may be sub-optimal, i.e. the characteristics of the value function satisfy (2.12–2.13), but there may be other solutions to these equations which are sub-optimal and therefore not characteristics of the value function. Optimality of solutions to the BVP can be guaranteed under certain convexity conditions, see e.g. [5, 14]. Addressing this challenging problem in a broader context is beyond the scope of the present work, but for the example problems we deal with, solutions of (2.12–2.13) also satisfy the sufficient conditions (see Section 3.3).

Even though solving the BVP is easier than solving the full HJB equation, we know of no general algorithm that is reliable and fast enough for real-time applications. However, in our approach the real-time feedback control computation is done by a NN which is trained *offline*. Thus we can solve the BVP offline to generate data for training and evaluating such a NN. For this purpose, numerically solving the BVP can be manageable although it may require some parameter tuning. In this paper, we use an implementation of the BVP solver introduced in [23]. This algorithm is based on a three-stage Lobatto IIIa discretization, a collocation formula which provides a solution that is fourth-order accurate. But the algorithm is highly sensitive to the initial guess for  $\mathbf{x}(t)$  and  $\boldsymbol{\lambda}(t)$ : there is no guarantee of convergence with an arbitrary initial guess. Furthermore, convergence is increasingly dependent on a good initializations as we increase the length of the time interval.

To overcome this difficulty, we employ the *time-marching* trick from [20, 21] in which the solution grows from an initially short time interval to the final time  $t_f$ . More specifically, we choose a time sequence

$$0 < t_1 < t_2 < \dots < t_K = t_f,$$

in which  $t_1$  is small. For the short time interval  $[0, t_1]$ , the BVP solver converges given most initial guesses near the initial state  $\mathbf{x}$ . Then the resulting trajectory is rescaled over

the longer time interval  $[0, t_2]$ . The rescaled trajectory is used as the initial guess to find a solution of the BVP for  $0 \leq t \leq t_2$ . We repeat this process until  $t_K = t_f$ , at which we obtain the full solution. Still, it is necessary to tune the time sequence  $\{t_k\}_{k=1}^K$  to achieve convergence while maintaining acceptable efficiency.

Computing many such solutions becomes expensive, which means that generating the large data sets necessary to train a NN can be difficult. With this in mind, we use the time-marching trick only to generate a small initial data set, and adaptively adding more points during training. The key to doing this efficiently is simulating the system dynamics using the partially-trained NN to close the loop. The closed-loop trajectory provides a good guess for the optimal state and costate over the entire time interval  $[0, t_f]$ , so that we can immediately solve (2.12–2.13) for all of  $[0, t_f]$ . Besides being more computationally efficient than time-marching, this approach also requires no parameter tuning. Details are presented in Section 4, and numerical comparisons between this method and the time-marching trick are given in Sections 5.2 and 6.2.

### 3 Neural network approximation of the value function

Neural networks have become a popular tool for modeling high-dimensional functions, since they are not dependent on discretizing the state space. In this paper, we apply NNs to approximate solutions of the HJB equation and evaluate the resulting feedback control in real-time. Specifically, we carry out the following steps:

1. *Initial data generation:* We compute the value function,  $V(t, \mathbf{x})$ , on trajectories  $\mathbf{x}(t)$  from initial conditions chosen by Monte Carlo sampling. Data is generated by solving the BVP as discussed in Section 2. In this initial data generation step, we require relatively few data points, since more data can be added later at little computational cost.
2. *Model training:* Given this data set, we train a NN to approximate the value function  $V(\cdot)$ . Learning is guided by the underlying structure of the problem, specifically by asking the NN to satisfy eq. (2.10). In doing so, we regularize the model and make efficient use out of small data sets.
3. *Adaptive data generation:* In the initial training phase we only have a small data set, so the NN only roughly approximates the value function. We now expand the data set by generating data in regions where the value function is likely to be steep or complicated, and thus difficult to learn. Computation of additional data is made efficient by good initial guesses obtained from NN-in-the-loop simulations of the system dynamics.
4. *Model refinement and validation:* We continue training the model and increasing the size of the data set until we satisfy some convergence criteria. Then, we check the generalization accuracy of the trained NN on a new set of validation data computed at Monte Carlo sample points.
5. *Feedback control:* We compute the optimal feedback control online by evaluating the gradient of the trained NN,  $V_{\mathbf{x}}^{NN}(\cdot)$ , and applying PMP. Notably, evaluation of the gra-

cient is extremely cheap even for large  $n$ , enabling implementation in high-dimensional systems.

The crux of the proposed method depends on modeling the value function (2.5) over a semi-global domain  $\mathcal{X} \subset \mathbb{R}^n$ . We present details of this process in the following subsections. In Section 3.1, we review the basic structure of feedforward NNs and describe how we train a NN to model the value function. Then in Section 3.2, we propose a simple way to incorporate information about the known problem structure into training. Finally in Section 3.3, we demonstrate how to use the trained NN for feedback control. The adaptive data generation scheme is treated separately in Section 4. The proposed method is illustrated in Section 5 by solving a practical optimal attitude control problem for a rigid body satellite, and then applied to solve larger problems in Section 6.

### 3.1 Feedforward neural networks

In this paper we use multilayer feedforward NNs. While many more sophisticated architectures have been developed for other applications, we find this basic architecture to be more than adequate for our purposes. Let  $V(\cdot)$  be the function we wish to approximate and  $V^{NN}(\cdot)$  be its NN representation. Feedforward NNs approximate complicated nonlinear functions by a composition of simpler functions, namely

$$V(t, \mathbf{x}) \approx V^{NN}(t, \mathbf{x}) = g_M \circ g_{M-1} \circ \cdots \circ g_1(t, \mathbf{x}),$$

where each layer  $g_m(\cdot)$  is just

$$g_m(\mathbf{y}) = \sigma_m(\mathbf{W}_m \mathbf{y} + \mathbf{b}_m).$$

Here  $\mathbf{W}_m$  and  $\mathbf{b}_m$  are the weight matrices and bias vectors, respectively.  $\sigma_m(\cdot)$  represents a nonlinear *activation function* applied component-wise to its argument; popular choices include ReLU, tanh, and other similar functions. In this paper, we use tanh for all the hidden layers. The final layer,  $g_M(\cdot)$ , is typically linear, so  $\sigma_M(\cdot)$  is the identity function.

Let  $\boldsymbol{\theta}$  denote the collection of the parameters of the NN, i.e.

$$\boldsymbol{\theta} := \{\mathbf{W}_m, \mathbf{b}_m\}_{m=1}^M.$$

The NN is trained by optimizing over the parameters  $\boldsymbol{\theta}$  to best approximate  $V(t, \mathbf{x})$  by  $V^{NN}(t, \mathbf{x}; \boldsymbol{\theta})$ . Specifically, by solving the BVP (2.12–2.13) from a set of randomly sampled initial conditions, we get a data set

$$\mathcal{D} = \{((t^{(i)}, \mathbf{x}^{(i)}), V^{(i)})\}_{i=1}^{N_d},$$

where  $(t^{(i)}, \mathbf{x}^{(i)})$  are the inputs,  $V^{(i)} := V(t^{(i)}, \mathbf{x}^{(i)})$  are the outputs to be modeled, and  $i = 1, 2, \dots, N_d$  are the indices of the data points. The NN is then trained by solving the nonlinear regression problem,

$$\underset{\boldsymbol{\theta}}{\text{minimize}} \frac{1}{N_d} \sum_{i=1}^{N_d} [V^{(i)} - V^{NN}(t^{(i)}, \mathbf{x}^{(i)}; \boldsymbol{\theta})]^2. \quad (3.1)$$



### 3.2 Physics-informed learning

Motivated by advances in physics-informed deep learning [28], we expect that we can improve on the rudimentary loss function in (3.1) by incorporating information about the underlying physics. In [28], and in particular in the context of HJB equations in [30] and [29], the known underlying PDE and boundary conditions are imposed by minimizing a residual loss over spatio-temporal collocation points. In this approach, no data is gathered: the PDE is solved directly in the least-squares sense. However, the residual must be evaluated over a large number of collocation points and can be rather expensive to compute. Thus we propose a simpler approach of modeling the costate  $\boldsymbol{\lambda}(\cdot)$  along with the value function itself, taking full advantage of the ability to gather data along the characteristics of the HJB PDE.

Specifically, we know that the costate must satisfy eq. (2.10), so we train the NN to minimize

$$\|\boldsymbol{\lambda}(t; \mathbf{x}) - V_{\mathbf{x}}^{NN}(t, \mathbf{x}; \boldsymbol{\theta})\|^2,$$

where  $V_{\mathbf{x}}^{NN}(\cdot)$  is the gradient of the NN representation of the value function with respect to the state. This quantity is calculated using automatic differentiation. In machine learning, automatic differentiation is usually used to compute gradients with respect to the model parameters, but is just as easy to apply to computing gradients with respect to inputs. In addition, the computational graph is pre-compiled so evaluating the gradient is cheap.

Costate data  $\boldsymbol{\lambda}(t)$  is obtained for each trajectory as a natural product of solving the BVP (2.12–2.13). Hence we have the augmented data set,

$$\bar{\mathcal{D}} = \{((t^{(i)}, \mathbf{x}^{(i)}), (V^{(i)}, \boldsymbol{\lambda}^{(i)}))\}_{i=1}^{N_d}, \quad (3.2)$$

where  $\boldsymbol{\lambda}^{(i)} := \boldsymbol{\lambda}(t^{(i)}; \mathbf{x}^{(i)})$ . We now define the *physics-informed learning problem*,

$$\begin{cases} \underset{\boldsymbol{\theta}}{\text{minimize}} & \mathcal{L}(\boldsymbol{\theta}; \bar{\mathcal{D}}), \\ \text{where} & \mathcal{L}(\boldsymbol{\theta}; \bar{\mathcal{D}}) := \text{loss}_V(\boldsymbol{\theta}; \bar{\mathcal{D}}) + \mu \cdot \text{loss}_{\boldsymbol{\lambda}}(\boldsymbol{\theta}; \bar{\mathcal{D}}). \end{cases} \quad (3.3)$$

Here  $\mu \geq 0$  is a scalar weight, the loss with respect to data is

$$\text{loss}_V(\boldsymbol{\theta}; \bar{\mathcal{D}}) := \frac{1}{N_d} \sum_{i=1}^{N_d} [V^{(i)} - V^{NN}(t^{(i)}, \mathbf{x}^{(i)}; \boldsymbol{\theta})]^2, \quad (3.4)$$

and the physics-informed gradient loss regularization is defined as

$$\text{loss}_{\boldsymbol{\lambda}}(\boldsymbol{\theta}; \bar{\mathcal{D}}) := \frac{1}{N_d} \sum_{i=1}^{N_d} \|\boldsymbol{\lambda}^{(i)} - V_{\mathbf{x}}^{NN}(t^{(i)}, \mathbf{x}^{(i)}; \boldsymbol{\theta})\|^2. \quad (3.5)$$

A NN trained to minimize (3.3) learns not just to fit the value data, but it is rewarded for doing so in a way that respects the underlying structure of the problem. This physics-informed regularization takes the known problem structure into account, so is preferable to the usual  $L^1$  or  $L^2$  regularization, which are based on the (heuristic) principle that simpler representations of data are likely to generalize better. Furthermore, we recall that the optimal control depends explicitly on  $V_{\mathbf{x}}(\cdot)$  – see Eqs. (2.11) and (3.6). Accurate approximation of



$V_{\mathbf{x}}(\cdot)$  is therefore essential for calculating optimal controls. Our method achieves this through automatic differentiation to compute *exact* gradients and by minimization of the physics-informed loss term (3.5).

In common practice, one usually randomly partitions the given data set (3.2) into a training set  $\bar{\mathcal{D}}_{\text{train}}$  and validation set  $\bar{\mathcal{D}}_{\text{val}}$ . During training, the loss functions (3.4) and (3.5) are calculated with respect to the training data  $\bar{\mathcal{D}}_{\text{train}}$ . We then evaluate the performance of the NN against the validation data  $\bar{\mathcal{D}}_{\text{val}}$ , which it did not observe during training. Good validation performance indicates that the NN generalizes well, i.e. it did not overfit the training data. We make the validation test more stringent by generating  $\bar{\mathcal{D}}_{\text{train}}$  and  $\bar{\mathcal{D}}_{\text{val}}$  from *independently drawn* initial conditions, so that the two data sets do not share any part of the same trajectories.

### 3.3 Neural network in the closed-loop system

Once the NN is trained, evaluating  $V_{\mathbf{x}}^{NN}(t, \mathbf{x})$  at new inputs is highly efficient. Moreover, since we minimized the gradient loss (3.5) during training, we also expect  $V_{\mathbf{x}}^{NN}(t, \mathbf{x})$  to approximate the true gradient well. At runtime, whenever the feedback control needs to be computed, we evaluate  $V_{\mathbf{x}}^{NN}(t, \mathbf{x})$  and then solve (2.11) based on this approximation.

For many problems of interest, the optimization problem (2.11) admits an analytic or semi-analytic solution. In particular, for the important class of control affine systems with running cost convex in  $\mathbf{u}$ , we can solve (2.11) analytically. Suppose that the system dynamics can be written in the form

$$\dot{\mathbf{x}} = \mathbf{f}(t, \mathbf{x}) + \mathbf{g}(t, \mathbf{x})\mathbf{u},$$

where  $\mathbf{f}(t, \mathbf{x}) : [0, t_f] \times \mathcal{X} \rightarrow \mathbb{R}^n$ ,  $\mathbf{g}(t, \mathbf{x}) : [0, t_f] \times \mathcal{X} \rightarrow \mathbb{R}^{n \times m}$ , and the control is unconstrained. Further, suppose that the running cost is of the form

$$L(t, \mathbf{x}, \mathbf{u}) = h(t, \mathbf{x}) + \mathbf{u}^T \mathbf{W} \mathbf{u},$$

for some function  $h(t, \mathbf{x}) : [0, t_f] \times \mathcal{X} \rightarrow \mathbb{R}$  and some positive definite weight matrix  $\mathbf{W} \in \mathbb{R}^{m \times m}$ . Then the Hamiltonian is

$$H(t, \mathbf{x}, \boldsymbol{\lambda}, \mathbf{u}) = h(t, \mathbf{x}) + \mathbf{u}^T \mathbf{W} \mathbf{u} + \boldsymbol{\lambda}^T \mathbf{f}(t, \mathbf{x}) + \boldsymbol{\lambda}^T \mathbf{g}(t, \mathbf{x})\mathbf{u}.$$

Now we apply PMP, which for unconstrained control requires

$$\mathbf{0}_{m \times 1} = \left. \frac{\partial H}{\partial \mathbf{u}} \right|_{\mathbf{u}=\mathbf{u}^*} = 2\mathbf{W}\mathbf{u}^* + \mathbf{g}^T(t, \mathbf{x})\boldsymbol{\lambda}.$$

Letting  $\boldsymbol{\lambda} = V_{\mathbf{x}}(t, \mathbf{x})$  and solving for  $\mathbf{u}^*$  yields the optimal feedback law,

$$\mathbf{u}^*(t, \mathbf{x}) = -\frac{1}{2}\mathbf{W}^{-1}\mathbf{g}^T(t, \mathbf{x})V_{\mathbf{x}}(t, \mathbf{x}). \quad (3.6)$$

**Remark 1** *For optimal control problems satisfying the above conditions, solutions to the BVP (2.12–2.13) are guaranteed to be optimal. This is because the Hessian of the Hamiltonian is*

$$H_{\mathbf{u}\mathbf{u}} = 2\mathbf{W},$$

*which is positive definite by assumption. Thus the second order sufficient conditions for optimality [5] are satisfied globally.*

## 4 Adaptive sampling and model refinement

Since generating just a single data point requires solving a challenging BVP, it can be expensive to generate large data sets which adequately represent the value function. This necessitates training using limited data and a method to generate new data in a smart and efficient way. In this paper, effective training with small data sets is accomplished by incorporating information about the costate as discussed in Section 3.2, but also by combining progressive batching with an efficient adaptive sampling technique.

Optimization methods in machine learning (see e.g. [4] for a comprehensive survey) are typically divided into second and first order methods. Second order methods like L-BFGS [7] rely on accurate gradient computations, and hence generally have to use the entire data set. For this reason they are often referred to as batch or full-batch methods. On the other hand, first order methods based on stochastic gradient descent (SGD) use only small subsets, or mini-batches, of the full data set. That is, at each optimization iteration  $k$ , the loss functions in (3.1) and (3.3) are evaluated only on a subset  $\mathcal{S}_k \subset \bar{\mathcal{D}}_{\text{train}}$  with  $|\mathcal{S}_k| \ll |\bar{\mathcal{D}}_{\text{train}}|$ . Here  $|\bar{\mathcal{D}}|$  denotes the number of data points in a data set  $\bar{\mathcal{D}}$ . Although second order methods converge much more quickly than first order methods, the necessary gradient calculations are prohibitively expensive for large data sets. Consequently, SGD variants have become the de facto standard for machine learning applications.

But in the context of deep learning, our NNs are small and data sets smaller. Thus we expect second order methods to be superior for our purposes. With a small initial data set, which we denote by  $\bar{\mathcal{D}}_{\text{train}}^1$ , we find that training a low-fidelity model is very fast using L-BFGS. After this initial round, we want to increase the size of the data set so that it better captures the features of the value function, then continue training the model (with more stringent convergence tolerances) using a larger data set,  $\bar{\mathcal{D}}_{\text{train}}^2$ . We continue this process until some conditions are satisfied.

Our approach is similar to and inspired by a progressive-batch method proposed in [6]. The primary difference is that the problem addressed in [6] is a standard machine learning problem, where a massive data set is available from the start. This allows one to increase the sample size every few iterations, and take a completely different sample from the available data. Our problem is different: we only have a small amount of data, but we can generate more as we go. However, data generation is expensive, so we would like to use and make only as much as is needed.

### 4.1 Convergence test and sample size selection

To start, suppose that the internal optimizer (e.g. L-BFGS) converges in optimization round  $r$ . Let  $\bar{\mathcal{D}}_{\text{train}}^r$  be the available training data set and  $\boldsymbol{\theta}_r$  denote the NN parameters at the end of this round. Given convergence of the internal optimizer, the first order necessary condition for optimality holds, so

$$\|\mathcal{L}_{\boldsymbol{\theta}}(\boldsymbol{\theta}_r; \bar{\mathcal{D}}_{\text{train}}^r)\| \ll 1. \quad (4.1)$$

Here  $\mathcal{L}(\cdot)$  is the physics-informed loss defined in eq. (3.3), and  $\mathcal{L}_{\boldsymbol{\theta}}(\cdot)$  is its gradient with respect to the NN parameters  $\boldsymbol{\theta}$ . For true first order optimality, we would like the gradient to be small when evaluated over the entire continuous domain of interest,  $[0, t_f] \times \mathcal{X}$ . In

other words, we want

$$\|\mathcal{L}_\theta(\boldsymbol{\theta}_r; [0, t_f] \times \mathcal{X})\| \ll 1, \quad (4.2)$$

where the Monte Carlo sums in Eqs. (3.4) and (3.5) become integrals in the limit as the size of the data set approaches infinity.

The simplest way to see if (4.2) holds is to generate a validation data set  $\bar{\mathcal{D}}_{\text{val}}$ . Then using the fact that  $\mathcal{L}_\theta(\boldsymbol{\theta}_r; \bar{\mathcal{D}}_{\text{val}}) \rightarrow \mathcal{L}_\theta(\boldsymbol{\theta}_r; [0, t_f] \times \mathcal{X})$  in the limit as  $|\bar{\mathcal{D}}_{\text{val}}| \rightarrow \infty$ , one checks if, for example,

$$\|\mathcal{L}_\theta(\boldsymbol{\theta}_r; \bar{\mathcal{D}}_{\text{val}})\| < \epsilon, \quad (4.3)$$

for some small parameter  $\epsilon > 0$ . Convergence tests like (4.3) are standard in machine learning, and are useful for measuring generalization accuracy. But for many practical problems including optimal control problems studied in this paper, it may be too expensive to generate a large-enough validation data set. More importantly, such tests provides no clear guidance in selecting the sample size  $|\bar{\mathcal{D}}_{\text{train}}^{r+1}|$  should they not be satisfied.

In this paper, we use validation tests to quantify model accuracy after training is complete. Indeed, the ability to empirically validate solutions is a key benefit of the causality-free approach. However, for the purpose of determining convergence between training rounds, we propose a different statistically motivated test which provides information on choosing  $|\bar{\mathcal{D}}_{\text{train}}^{r+1}|$ . The idea is simple: since we already assume (4.1) holds, then to ensure that (4.2) is also satisfied, it suffices to check that the population variance is relatively small.

To motivate this more rigorously, we observe that – by design – for any sample set  $\bar{\mathcal{D}}$ , the sample gradient  $\mathcal{L}_\theta(\boldsymbol{\theta}_r; \bar{\mathcal{D}})$  is an unbiased estimator for the true gradient. That is,

$$\mathbb{E}_{\bar{\mathcal{D}}}[\mathcal{L}_\theta(\boldsymbol{\theta}_r; \bar{\mathcal{D}})] = \mathcal{L}_\theta(\boldsymbol{\theta}_r; [0, t_f] \times \mathcal{X}),$$

where  $\mathbb{E}_{\bar{\mathcal{D}}}[\cdot]$  denotes the population mean over all possible sample sets  $\bar{\mathcal{D}}$  with fixed size  $|\bar{\mathcal{D}}|$ . Intuitively, this means that if (4.1) holds, then on average we also have (4.2), as desired. But we must control the mean square error (MSE) of the estimator, which is given by

$$\begin{aligned} \text{MSE}[\mathcal{L}_\theta(\boldsymbol{\theta}_r; \bar{\mathcal{D}})] &:= \mathbb{E}_{\bar{\mathcal{D}}} \left[ \|\mathcal{L}_\theta(\boldsymbol{\theta}_r; \bar{\mathcal{D}}) - \mathcal{L}_\theta(\boldsymbol{\theta}_r; [0, t_f] \times \mathcal{X})\|^2 \right] \\ &= \mathbb{E}_{\bar{\mathcal{D}}} \left[ \sum_{m=1}^M \left( \frac{\partial \mathcal{L}}{\partial \theta_m}(\boldsymbol{\theta}_r; \bar{\mathcal{D}}) - \frac{\partial \mathcal{L}}{\partial \theta_m}(\boldsymbol{\theta}_r; [0, t_f] \times \mathcal{X}) \right)^2 \right]. \end{aligned} \quad (4.4)$$

Now by linearity of the expectation we have

$$\text{MSE}[\mathcal{L}_\theta(\boldsymbol{\theta}_r; \bar{\mathcal{D}})] = \sum_{m=1}^M \text{Var} \left[ \frac{\partial \mathcal{L}}{\partial \theta_m}(\boldsymbol{\theta}_r; \bar{\mathcal{D}}) \right],$$

and then by construction of the loss function,

$$\text{MSE}[\mathcal{L}_\theta(\boldsymbol{\theta}_r; \bar{\mathcal{D}})] = \sum_{m=1}^M \text{Var} \left[ \frac{1}{|\bar{\mathcal{D}}|} \sum_{i=1}^{|\bar{\mathcal{D}}|} \frac{\partial \mathcal{L}}{\partial \theta_m}(\boldsymbol{\theta}_r; (t^{(i)}, \mathbf{x}^{(i)})) \right].$$

Using the fact that the samples  $(t^{(i)}, \mathbf{x}^{(i)})$  are independent and identically distributed, we get

$$\begin{aligned} \text{MSE} [\mathcal{L}_\theta (\boldsymbol{\theta}_r; \bar{\mathcal{D}})] &= \frac{1}{|\bar{\mathcal{D}}|^2} \sum_{m=1}^M \sum_{i=1}^{|\bar{\mathcal{D}}|} \text{Var} \left[ \frac{\partial \mathcal{L}}{\partial \theta_m} (\boldsymbol{\theta}_r; (t, \mathbf{x})) \right] \\ &= \frac{1}{|\bar{\mathcal{D}}|^2} \sum_{m=1}^M |\bar{\mathcal{D}}| \text{Var} \left[ \frac{\partial \mathcal{L}}{\partial \theta_m} (\boldsymbol{\theta}_r; (t, \mathbf{x})) \right] \\ &= \frac{1}{|\bar{\mathcal{D}}|} \sum_{m=1}^M \text{Var} \left[ \frac{\partial \mathcal{L}}{\partial \theta_m} (\boldsymbol{\theta}_r; (t, \mathbf{x})) \right], \end{aligned} \quad (4.5)$$

where  $M$  is the number of parameters  $\boldsymbol{\theta}$ . If the estimation error is small, then the sample mean is likely to be a good approximation of the true mean. Hence we expect that  $\|\mathcal{L}_\theta (\boldsymbol{\theta}_r; [0, t_f] \times \mathcal{X})\|$  is also small, as desired. To this end, we require

$$\text{MSE} [\mathcal{L}_\theta (\boldsymbol{\theta}_r; \bar{\mathcal{D}})] \leq \epsilon \|\mathcal{L}_\theta (\boldsymbol{\theta}_r; [0, t_f] \times \mathcal{X})\|_1, \quad (4.6)$$

for some parameter  $\epsilon > 0$ .

In practice, evaluation of (4.6) is computationally intractable, but we can approximate the true population variance terms on the left hand side by the *sample* variance<sup>1</sup> taken over all data  $(t^{(i)}, \mathbf{x}^{(i)}) \in \bar{\mathcal{D}}_{\text{train}}^r$ , which we denote by  $\text{Var}_{\bar{\mathcal{D}}_{\text{train}}^r} [\cdot]$ :

$$\text{MSE} [\mathcal{L}_\theta (\boldsymbol{\theta}_r; \bar{\mathcal{D}})] \approx \frac{1}{|\bar{\mathcal{D}}_{\text{train}}^r|} \sum_{m=1}^M \text{Var}_{\bar{\mathcal{D}}_{\text{train}}^r} \left[ \frac{\partial \mathcal{L}}{\partial \theta_m} (\boldsymbol{\theta}_r; (t^{(i)}, \mathbf{x}^{(i)})) \right].$$

Similarly, we approximate the true gradient on the right hand side by the sample gradient and arrive at the following practical convergence criterion:

$$\sum_{m=1}^M \text{Var}_{\bar{\mathcal{D}}_{\text{train}}^r} \left[ \frac{\partial \mathcal{L}}{\partial \theta_m} (\boldsymbol{\theta}_r; (t^{(i)}, \mathbf{x}^{(i)})) \right] \leq \epsilon |\bar{\mathcal{D}}_{\text{train}}^r| \|\mathcal{L}_\theta (\boldsymbol{\theta}_r; \bar{\mathcal{D}}_{\text{train}}^r)\|_1. \quad (4.7)$$

If (4.7) is satisfied, then it is likely that  $\|\mathcal{L}_\theta (\boldsymbol{\theta}_r; [0, t_f] \times \mathcal{X})\|$  is small. In other words, the solution  $\boldsymbol{\theta}_r$  should satisfy the first order optimality conditions evaluated over the entire domain, so we can stop optimization. Satisfaction of (4.7) does not imply that the trained model is good – merely that seeing more data would probably not improve it significantly. On the other hand, when the criterion is not met, it still guides us in selecting the next sample size  $|\bar{\mathcal{D}}_{\text{train}}^{r+1}|$ . To see this, suppose that the sample variance doesn't change significantly by increasing the size of the data set, i.e.

$$\frac{\sum_{m=1}^M \text{Var}_{\bar{\mathcal{D}}_{\text{train}}^{r+1}} \left[ \frac{\partial \mathcal{L}}{\partial \theta_m} (\boldsymbol{\theta}_r; (t^{(i)}, \mathbf{x}^{(i)})) \right]}{\|\mathcal{L}_\theta (\boldsymbol{\theta}_r; \bar{\mathcal{D}}_{\text{train}}^{r+1})\|_1} \approx \frac{\sum_{m=1}^M \text{Var}_{\bar{\mathcal{D}}_{\text{train}}^r} \left[ \frac{\partial \mathcal{L}}{\partial \theta_m} (\boldsymbol{\theta}_r; (t^{(i)}, \mathbf{x}^{(i)})) \right]}{\|\mathcal{L}_\theta (\boldsymbol{\theta}_r; \bar{\mathcal{D}}_{\text{train}}^r)\|_1}.$$

---

<sup>1</sup>In practice, computing a large number of individual gradients can be expensive, so we often evaluate the sample variance over a smaller subset of the training data.

Then the appropriate choice of  $|\bar{\mathcal{D}}_{\text{train}}^{r+1}|$  to satisfy (4.7) after the next round is such that

$$|\bar{\mathcal{D}}_{\text{train}}^{r+1}| \geq \frac{\sum_{m=1}^M \text{Var}_{\bar{\mathcal{D}}_{\text{train}}^r} \left[ \frac{\partial \mathcal{L}}{\partial \theta_m} (\boldsymbol{\theta}_r; (t^{(i)}, \mathbf{x}^{(i)})) \right]}{\epsilon \|\mathcal{L}_{\boldsymbol{\theta}} (\boldsymbol{\theta}_r; \bar{\mathcal{D}}_{\text{train}}^r)\|_1}. \quad (4.8)$$

**Remark 2** *The convergence test (4.7) and sample size selection scheme (4.8) derived above are not specific to learning solutions to the HJB equation. They can be applied to many data-driven optimization problems where data is scarce but can be generated over time. Notably, these results facilitate the use of existing algorithms for second order and constrained optimization in such applications.*

## 4.2 Adaptive data generation with NN warm start

The sample size selection criterion (4.8) we propose indicates how many data are necessary to satisfy the convergence test (4.7), assuming a uniform sampling from the domain. In practice, since all the data we generate will be new, we can choose to generate new data where it is needed most, hence the term *adaptive sampling*. This condition for generating new data can be interpreted in many ways. In this paper, we concentrate samples where  $\|V_{\mathbf{x}}^{NN}(\cdot)\|$  is large. Regions of the value function with large gradients tend to be steep or complicated, and thus may benefit from having more data to learn from.

Specifically, for each initial condition we want to integrate, we can first randomly sample a set of  $N_c$  candidate initial conditions from  $\mathcal{X}$ . A quick pass through the NN yields the predicted gradient at all candidate points:

$$\left\{ V_{\mathbf{x}}^{NN} \left( 0, \mathbf{x}_0^{(i)} \right) \right\}_{i=1}^{N_c}.$$

Instead of using the time-marching trick described in Section 2, we simulate the system dynamics using the partially-trained NN as the closed-loop controller. In most cases, this yields an approximate solution which is reasonably close to the optimal state  $\mathbf{x}^*(t)$  and costate  $\boldsymbol{\lambda}(t)$ . By supplying this trajectory as an initial guess to the BVP solver, we then quickly and reliably obtain a solution to the BVP for the full time interval  $[0, t_f]$ . This process is repeated for new initial conditions until we obtain the desired amount of data (each trajectory may contain hundreds of data points). We refer to this technique as a *NN warm start*. A summary of the full training procedure is given in Algorithm 1.

This algorithm enables us to build up a rich data set and a high-fidelity model of  $V(\cdot)$ . Moreover, the data set is not constrained to lie within a small neighborhood of some nominal trajectory. It can contain points from the entire domain of  $\mathcal{X}$ , and we can adjust the process as described to generate more data near complicated features of the value function. As we progressively refine the NN model, we can adjust the gradient loss weight  $\mu$  or other hyperparameters such as the internal optimizer convergence tolerance and the number of terms in the L-BFGS Hessian approximation. As the NN is already partially-trained, fewer iterations should be needed for convergence in each round so we can afford to make each iteration more expensive.

---

**Algorithm 1** Adaptive sampling and model refinement

---

```
1: Generate  $\bar{\mathcal{D}}_{\text{train}}^1$  using time-marching
2: for  $r = 1, 2, \dots$  do
3:   Solve (3.3) for  $\theta_r$ 
4:   if (4.7) is satisfied then
5:     return optimized parameters  $\theta_r$  and NN validation accuracy
6:   else
7:     while (4.8) is not satisfied do
8:       Sample initial conditions  $\mathbf{x}_0^{(i)}$ ,  $i = 1, \dots, N_c$ , from  $\mathcal{X}$ 
9:       In parallel, predict  $\left\| V_{\mathbf{x}}^{NN} \left( 0, \mathbf{x}_0^{(i)} \right) \right\|$ ,  $i = 1, \dots, N_c$ 
10:      Choose the initial condition with largest gradient norm and use NN warm start
      to solve the BVP (2.12–2.13)
11:      Add the resulting trajectory to  $\bar{\mathcal{D}}_{\text{train}}^{r+1}$ 
12:    end while
13:  end if
14: end for
```

---

## 5 Application to rigid body satellite rotation

As a practical test of our proposed method, we consider the six-state rigid body model of a satellite studied by Kang and Wilcox [20, 21]. With the sparse grid characteristics method, they interpolate the value function at initial time,  $V(t = 0, \mathbf{x})$ , and use this for model predictive feedback control (MPC) of the nonlinear system. We use their successful results as a baseline for evaluating our method.

Let  $\{\mathbf{e}_1, \mathbf{e}_2, \mathbf{e}_3\}$  be an inertial frame of orthonormal vectors and let  $\{\mathbf{e}'_1, \mathbf{e}'_2, \mathbf{e}'_3\}$  be a body frame. The state of the satellite is then written as  $\mathbf{x} = (\mathbf{v} \ \boldsymbol{\omega})^T$ . Here  $\mathbf{v}$  is the attitude of the satellite represented in Euler angles,

$$\mathbf{v} = (\phi \ \theta \ \psi)^T,$$

in which  $\phi$ ,  $\theta$ , and  $\psi$  are the angles of rotation around  $\mathbf{e}'_1$ ,  $\mathbf{e}'_2$ , and  $\mathbf{e}'_3$ , respectively, in the order (3, 2, 1) – see [11] – and  $\boldsymbol{\omega}$  is the angular velocity in the body frame,

$$\boldsymbol{\omega} = (\omega_1 \ \omega_2 \ \omega_3)^T.$$

The state dynamics are

$$\begin{pmatrix} \dot{\mathbf{v}} \\ \mathbf{J}\dot{\boldsymbol{\omega}} \end{pmatrix} = \begin{pmatrix} \mathbf{E}(\mathbf{v})\boldsymbol{\omega} \\ \mathbf{S}(\boldsymbol{\omega})\mathbf{R}(\mathbf{v})\mathbf{h} + \mathbf{B}\mathbf{u} \end{pmatrix}.$$

Here  $\mathbf{E}(\mathbf{v})$ ,  $\mathbf{S}(\boldsymbol{\omega})$ ,  $\mathbf{R}(\mathbf{v}) : \mathbb{R}^3 \rightarrow \mathbb{R}^{3 \times 3}$  are matrix-valued functions defined as

$$\mathbf{E}(\mathbf{v}) := \begin{pmatrix} 1 & \sin \phi \tan \theta & \cos \phi \tan \theta \\ 0 & \cos \phi & -\sin \phi \\ 0 & \sin \phi / \cos \theta & \cos \phi / \cos \theta \end{pmatrix}, \quad \mathbf{S}(\boldsymbol{\omega}) := \begin{pmatrix} 0 & \omega_3 & -\omega_2 \\ -\omega_3 & 0 & \omega_1 \\ \omega_2 & -\omega_1 & 0 \end{pmatrix},$$

and

$$\mathbf{R}(\mathbf{v}) := \begin{pmatrix} \cos \theta \cos \psi & \cos \theta \sin \psi & -\sin \theta \\ \sin \phi \sin \theta \cos \psi - \cos \phi \sin \psi & \sin \phi \sin \theta \sin \psi + \cos \phi \cos \psi & \cos \theta \sin \phi \\ \cos \phi \sin \theta \cos \psi + \sin \phi \sin \psi & \cos \phi \sin \theta \sin \psi - \sin \phi \cos \psi & \cos \theta \cos \phi \end{pmatrix}.$$

Further,  $\mathbf{J} \in \mathbb{R}^{3 \times 3}$  is a combination of the inertia matrices of the momentum wheels and the rigid body without wheels,  $\mathbf{h} \in \mathbb{R}^3$  is the total constant angular momentum of the system, and  $\mathbf{B} \in \mathbb{R}^{3 \times m}$  is a constant matrix where  $m$  is the number of momentum wheels. To control the system, we apply a torque  $\mathbf{u}(t, \mathbf{v}, \boldsymbol{\omega}) : [0, t_f] \times \mathbb{R}^3 \times \mathbb{R}^3 \rightarrow \mathbb{R}^m$ .

We consider the fully-actuated case where  $m = 3$ . Let

$$\mathbf{B} = \begin{pmatrix} 1 & 1/20 & 1/10 \\ 1/15 & 1 & 1/10 \\ 1/10 & 1/15 & 1 \end{pmatrix}, \quad \mathbf{J} = \begin{pmatrix} 2 & 0 & 0 \\ 0 & 3 & 0 \\ 0 & 0 & 4 \end{pmatrix}, \quad \mathbf{h} = \begin{pmatrix} 1 \\ 1 \\ 1 \end{pmatrix}.$$

The optimal control problem is

$$\begin{cases} \underset{\mathbf{u}(\cdot)}{\text{minimize}} & \int_t^{t_f} L(\mathbf{v}, \boldsymbol{\omega}, \mathbf{u}) d\tau + \frac{W_4}{2} \|\mathbf{v}(t_f)\|^2 + \frac{W_5}{2} \|\boldsymbol{\omega}(t_f)\|^2, \\ \text{subject to} & \dot{\mathbf{v}} = \mathbf{E}(\mathbf{v})\boldsymbol{\omega}, \\ & \mathbf{J}\dot{\boldsymbol{\omega}} = \mathbf{S}(\boldsymbol{\omega})\mathbf{R}(\mathbf{v})\mathbf{h} + \mathbf{B}\mathbf{u}. \end{cases} \quad (5.1)$$

Here

$$L(\mathbf{v}, \boldsymbol{\omega}, \mathbf{u}) = \frac{W_1}{2} \|\mathbf{v}\|^2 + \frac{W_2}{2} \|\boldsymbol{\omega}\|^2 + \frac{W_3}{2} \|\mathbf{u}\|^2,$$

and

$$W_1 = 1, \quad W_2 = 10, \quad W_3 = \frac{1}{2}, \quad W_4 = 1, \quad W_5 = 1, \quad t_f = 20.$$

We sample  $N_d$  initial values  $\{(\mathbf{v}^{(i)}, \boldsymbol{\omega}^{(i)})\}_{i=1}^{N_d}$  from the domain

$$\mathcal{X}_0 = \left\{ \mathbf{v}, \boldsymbol{\omega} \in \mathbb{R}^3 \mid -\frac{\pi}{3} \leq \phi, \theta, \psi \leq \frac{\pi}{3} \text{ and } -\frac{\pi}{4} \leq \omega_1, \omega_2, \omega_3 \leq \frac{\pi}{4} \right\},$$

and solve the two-point BVP (2.12–2.13) at each initial value  $(\mathbf{v}^{(i)}, \boldsymbol{\omega}^{(i)})$ ,  $i = 1, \dots, N_d$ , using the SciPy [17] implementation of the three-stage Lobatto IIIa algorithm in [23]. In [21], the value function is approximated only at initial time  $t = 0$ , so to facilitate comparison we do the same. This means that the system is controlled for the whole time interval  $t \in [0, 20]$  by  $\mathbf{u}^{NN}(0, \mathbf{v}, \boldsymbol{\omega})$ . Consequently, the control is actually implemented as MPC rather than time-dependent optimal control. In other words, at each time  $t$  when the integrator needs to evaluate the control, instead of computing  $\mathbf{u}^{NN}(t, \mathbf{v}, \boldsymbol{\omega})$ , we let  $t = 0$  and return  $\mathbf{u}^{NN}(0, \mathbf{v}, \boldsymbol{\omega})$ . This is justifiable because the optimal control problem (5.1) is time-invariant.

## 5.1 Learning the value function

In this section, we present numerical results of our implementation of a NN for modeling the value function of the rigid body attitude control problem (5.1). In [21], the value function is



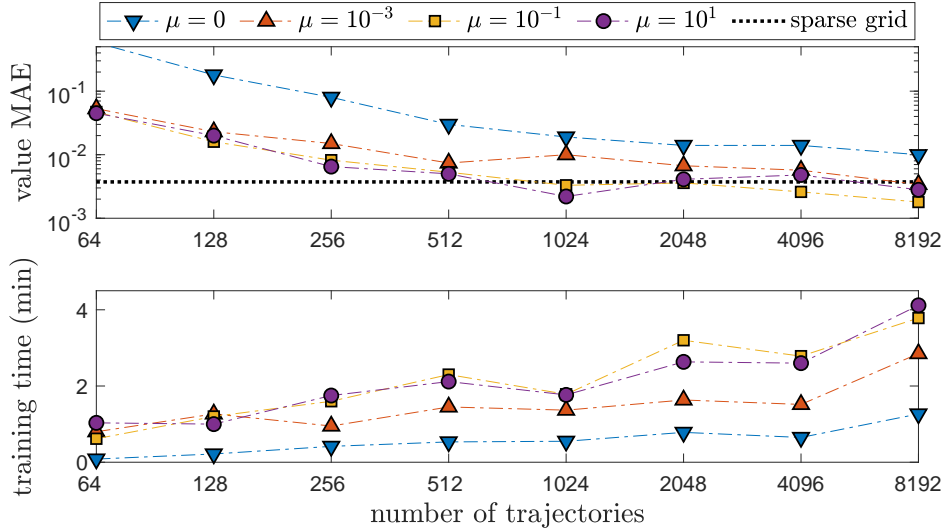


Figure 1: Validation accuracy and training time of NNs for modeling initial time value function  $V(0, \mathbf{v}, \boldsymbol{\omega})$  of the rigid body optimal attitude control problem (5.1). All NNs have the same parameter initialization and are run on an NVIDIA RTX 2080Ti GPU.

approximated only at  $t = 0$  to avoid discretizing time in addition to space. Thus to facilitate a fair comparison, we also approximate the value function at initial time only.

To obtain data for training and validation, we solve the two-point BVP (2.12–2.13) at initial conditions sampled uniformly from  $\mathcal{X}_0$ . We solve each BVP using time-marching and the SciPy [17] implementation of the three-stage Lobatto IIIa algorithm in [23]. Each integrated trajectory contains around 100 data points on average, but we use only initial time data,  $V(0, \mathbf{v}, \boldsymbol{\omega})$ . For validation, we generate a data set containing  $|\mathcal{D}_{\text{val}}| = 1000$  data points (at  $t = 0$ ), and keep this fixed throughout all the tests. As a baseline, the sparse grid characteristics method with  $|G_{\text{sparse}}^{13}| = 44,698$  grid points achieves a mean absolute error (MAE) of  $3.7 \times 10^{-3}$  on this data set.

We implement a standard feedforward NN in TensorFlow [1] and train it to approximate  $V(0, \mathbf{v}, \boldsymbol{\omega})$ . The NN has three hidden layers with 64 neurons in each, but many alternate configurations of depth and width also work. For optimization, we use the SciPy interface for the L-BFGS optimizer [17, 7]. We experiment with changing the number of training data and the weight  $\mu$  on the value gradient loss term (3.5), and compare the results to those obtained in [21]. Notably, we demonstrate that we can beat the accuracy of the sparse grid characteristics method while using about 40 times fewer sample trajectories.

Figure 1 displays the results of a series of tests in which we vary the gradient loss weight  $\mu$  and the size of the training data set. We highlight that with just 1024 data points, we can obtain NNs with better accuracy than the sparse grid characteristics method with  $|G_{\text{sparse}}^{13}| = 44,698$  points. For this problem, best results are obtained by choosing  $\mu$  between  $10^{-1}$  and  $10^1$ . With 8192 data points, the trained NN is twice as accurate as the sparse grid characteristics method. This level of accuracy with small data sets is obtained only with physics-informed learning. In particular, NNs trained by pure regression (3.1) cannot match the accuracy of the sparse grid characteristics method, as shown in Figure 1 for the case with

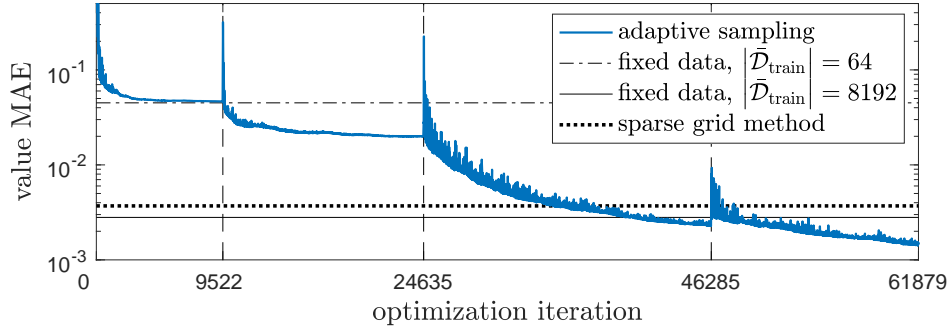


Figure 2: Progress of adaptive sampling and model refinement for the rigid body problem (5.1), compared to training on fixed data sets and the sparse grid characteristics method. Vertical dashed lines show the start of new training rounds.

$\mu = 0$ . While physics-informed learning is more costly, it permits the use of much smaller data sets, and the increased training time is still quite short.

## 5.2 Training with adaptive data generation

Performing a thorough systematic study of the adaptive sampling and model refinement technique proposed in Section 4 is rather complicated, since a successful implementation depends on various hyperparameter settings, which can and perhaps should change each optimization round. Results also depend on random chance, since data points are chosen in a (partially) random way and the randomly-initialized NN training problem is highly non-convex. For this reason, in this section we show a just few conservative results which we feel demonstrate the potential of the method.

Figure 2 shows the progress of the validation error during training when using adaptive sampling starting from a data set with  $|\bar{\mathcal{D}}_{\text{train}}^1| = 64$  points. This is the same data set with 64 points used in Section 5.1. We set the gradient loss weight  $\mu = 10$  and the convergence tolerance in (4.7) to  $\epsilon = 0.1$ . After each round, we check the convergence criterion (4.7) and increase the number of training data to the smallest power of 2 which is larger than the number of points recommended by (4.8). With these configurations, the model passes the convergence test after 4 training rounds, and the data set sizes selected are  $|\bar{\mathcal{D}}_{\text{train}}^2| = 128$ ,  $|\bar{\mathcal{D}}_{\text{train}}^3| = 1024$ , and  $|\bar{\mathcal{D}}_{\text{train}}^4| = 4096$ . Each data set includes all previously generated data, and we generate additional data as needed through Algorithm 1.

Results are compared to the progress when training on fixed data sets with  $|\bar{\mathcal{D}}_{\text{train}}| = 64$  and 8192 points (the same as used in Section 5.1). Even with a naïve implementation, the final accuracy is better than that obtained when training on a fixed data set with  $|\bar{\mathcal{D}}_{\text{train}}| = 8192$ , even though training started with only  $|\bar{\mathcal{D}}_{\text{train}}^1| = 64$  points. These results highlight the advantage of the adaptive sampling and model refinement method: the ability to overcome an initial lack of data. To fully realize the potential of the method, hyperparameters like  $\mu$ ,  $\epsilon$  and internal optimizer parameters need to be adjusted in each round. Development of algorithms to do this adaptively is beyond the scope of this paper, and remains a topic for future research.

Next, we investigate the convergence of the BVP solver with time-marching and NN

$K$	% BVP convergence	mean integration time
1	0.3%	0.37 s
2	38.7%	0.44 s
3	76.2%	0.40 s
4	92.9%	0.45 s
8	98.4%	0.53 s

Table 1: Convergence of BVP solutions for (5.1) when using the time-marching trick, depending on the number of steps in the sequence  $\{t_k\}_{k=1}^K$ . The case  $K = 1$  corresponds to a direct solution attempt over the whole time interval with no time-marching. BVP integration time is measured only on successful attempts – failed solution attempts usually take much longer.

$\mu$	gradient $MRL^2$	% BVP conv.	mean int. time
0	$3.7 \times 10^{-1}$	90%	0.44 s
$10^{-3}$	$4.0 \times 10^{-2}$	99.6%	0.41 s
$10^1$	$3.5 \times 10^{-2}$	100%	0.40 s

Table 2: Convergence of BVP solutions for (5.1) when using NN warm start with NNs of varying gradient prediction accuracy. BVP integration time is measured only on successful attempts.

warm start. Results are given in Table 1 and Table 2, respectively. For these tests, we use 1000 initial conditions with the largest predicted gradient norm,  $\|V_{\mathbf{x}}^{NN}(\cdot)\|$ , picked from a set of  $10^6$  randomly sampled candidate points. Initial conditions with large gradient norm tend to be located in regions where the value function is steep or complicated, and may thus be more difficult to solve. The set of initial conditions is fixed for all tests.

In the first row of Table 1, we attempt to solve the BVP with no time-marching, i.e. over the entire time interval without constructing any initial guess. In this case, the proportion of convergent solutions is extremely small, obviating the need for good initial guesses. As shown in Table 1, we reliably obtain solutions for this problem when we use at least  $K = 4$  time intervals. We note that the initial conditions are purposefully chosen to be difficult – if we simply take random samples from the domain  $\mathcal{X}_0$ , the proportion of convergent solutions increases significantly.

In Table 2, we present results using NN warm start. The NNs are trained on a data set of 64 trajectories, but with different weights  $\mu$ . They therefore have varying accuracy in predicting the costate,  $\boldsymbol{\lambda}(0; \mathbf{x}) \approx V_{\mathbf{x}}^{NN}(0, \mathbf{x})$ , measured as mean relative  $L^2$  error ( $MRL^2$ ). Accurate computation of the costate is key to synthesis of good optimal controls. We observe that using even a low-fidelity NN (first row of Table 2), the rate of BVP convergence is just as high as when using  $K = 4$  time intervals for time-marching. The quality of initial guesses improves with better costate prediction, and it is not difficult to exceed 99% convergence. NN warm start solutions are also faster than equivalently reliable solutions obtained with time-marching. While the difference is negligible for individual trajectories, considerable time savings can be realized when building large data sets or solving more difficult high-dimensional BVPs. This is further explored in Section 6.2.

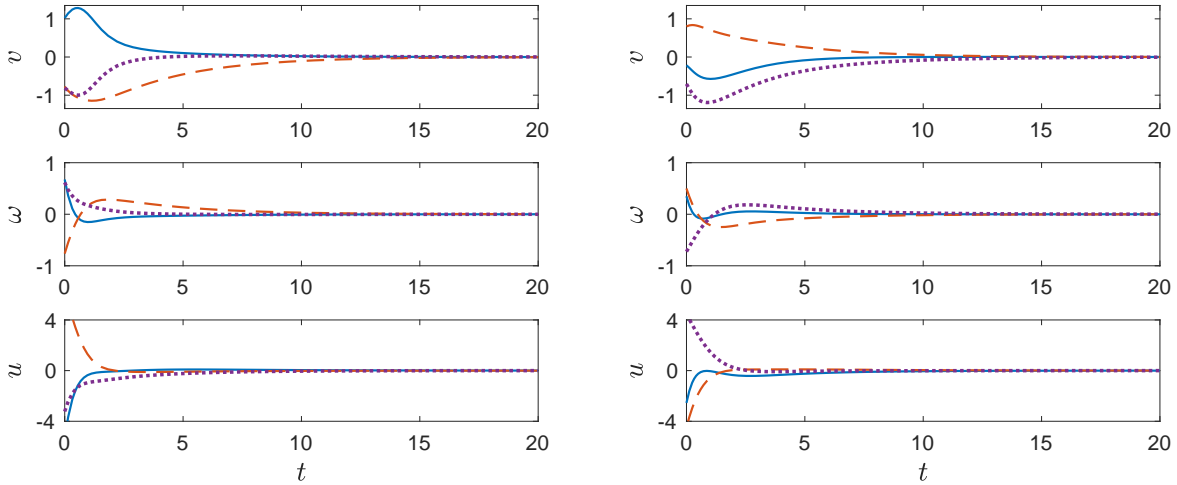


Figure 3: Sample closed-loop trajectories of the rigid body system controlled by NN model predictive feedback. Solid:  $\phi$ ,  $\omega_1$ , and  $u_1$ . Dashed:  $\theta$ ,  $\omega_2$ , and  $u_2$ . Dotted:  $\psi$ ,  $\omega_3$ , and  $u_3$ .

### 5.3 Closed-loop simulations

In this section we perform numerical simulations of the rigid body dynamics, demonstrating that the NN feedback controller is capable of stabilizing the system. Using (3.6) we calculate the optimal feedback control law

$$\mathbf{u}^{NN}(t, \mathbf{v}, \boldsymbol{\omega}) = -\frac{1}{W_3} [\mathbf{J}^{-1}\mathbf{B}]^T V_{\boldsymbol{\omega}}^{NN}(t, \mathbf{v}, \boldsymbol{\omega}). \quad (5.2)$$

Since  $\mathbf{J}$  and  $\mathbf{B}$  are constant matrices, we pre-compute the product  $-\mathbf{J}^{-1}\mathbf{B}^T/W_3$ . Hence evaluation of the control requires only a forward pass through the computational graph of the gradient  $V_{\boldsymbol{\omega}}^{NN}(\cdot)$  and a matrix multiplication. Recall that for this problem we implement MPC, i.e.  $\mathbf{u} = \mathbf{u}^{NN}(0, \mathbf{v}, \boldsymbol{\omega})$  for all  $t \in [0, 20]$ . Thus the control may be sub-optimal, but we find that it still performs well.

In Figure 3, we plot two typical closed-loop trajectories starting from randomly sampled initial conditions. We choose these initial conditions to have large predicted gradient norm to make the problem more difficult. Still, we can clearly see that the NN controller asymptotically stabilizes these trajectories. We also note that short computation time is critical for implementation in real systems, and this is achieved here as each evaluation of the control needs only  $O(10^{-3})$  seconds on both an NVIDIA RTX 2080Ti GPU and a 2012 MacBook Pro.

## 6 Application to control of Burgers'-type PDE

In this section, we test our method on high-dimensional nonlinear systems of ODEs arising from Chebyshev pseudospectral (PS) discretization of a one-dimensional forced Burgers'-type PDE. An infinite-horizon version of this problem is studied in [18], in which the value function is approximated by a polynomial. We note that in [18], separability of the nonlinear

dynamics is required to compute the high-dimensional integrals necessary in the Galerkin formulation. Our method does not require this restriction, although it does apply in this problem.

As in [18], let  $X(t, \xi) : [0, t_f] \times [-1, 1] \rightarrow \mathbb{R}$  satisfy the following one-dimensional PDE with Dirichlet boundary conditions:

$$\begin{cases} X_t = XX_\xi + \nu X_{\xi\xi} + \alpha X e^{\beta X} + I_\Omega(\xi)u, & t > 0, \xi \in (-1, 1), \\ X(t, -1) = X(t, 1) = 0, & t > 0, \\ X(0, \xi) = X_0, & \xi \in (-1, 1). \end{cases} \quad (6.1)$$

For notational convenience we have written  $X = X(t, \xi)$ . As before, we denote  $X_t = \partial X / \partial t$ ,  $X_\xi = \partial X / \partial \xi$ , and  $X_{\xi\xi} = \partial^2 X / \partial \xi^2$ . The control  $u(t, X) : [0, t_f] \times \mathbb{R} \rightarrow \mathbb{R}$  is actuated only on  $\Omega$ , the support of the indicator function  $I_\Omega(\xi) : [-1, 1] \rightarrow \{0, 1\}$ , which is defined as

$$I_\Omega(\xi) = \begin{cases} 1, & \xi \in \Omega, \\ 0, & \xi \notin \Omega. \end{cases}$$

The optimal control problem we consider is

$$\begin{cases} \underset{u(\cdot)}{\text{minimize}} & \int_t^{t_f} L(X, u) d\tau + \frac{W_2}{2} \|X(t_f, \xi)\|_{L^2_{(-1,1)}}^2, \\ \text{subject to} & X_t = XX_\xi + \nu X_{\xi\xi} + \alpha X e^{\beta X} + I_\Omega(\xi)u, \\ & X(\tau, -1) = X(\tau, 1) = 0. \end{cases} \quad (6.2)$$

Here

$$L(X, u) = \frac{1}{2} \|X(\tau, \xi)\|_{L^2_{(-1,1)}}^2 + \frac{W_1}{2} u^2(\tau, X), \quad \|X(\tau, \xi)\|_{L^2_{(-1,1)}}^2 := \int_{-1}^1 |X(\tau, \xi)|^2 d\xi,$$

and we set

$$\Omega = (-0.5, -0.2), \quad \nu = 0.2, \quad \alpha = 1.5, \quad \beta = -0.1, \quad W_1 = 0.1, \quad W_2 = 1, \quad t_f = 8.$$

In this problem, the goal of stabilizing  $X(t, \xi)$  is made more challenging by the added source term,  $\alpha X e^{\beta X}$ , which renders the origin unstable. This can be seen clearly in Figure 4a.

To solve (6.2) using our framework, we perform Chebyshev PS collocation to transform the PDE (6.1) into a system of ODEs. Following [31], we let

$$\xi_j = \cos(j\pi/N_c), \quad j = 0, 1, \dots, N_c,$$

where  $N_c + 1$  is the number of collocation points. After accounting for boundary conditions, we collocate  $X(t, \xi)$  at internal (non-boundary) Chebyshev points,  $\xi_j$ ,  $j = 1, 2, \dots, n$ , where  $n = N_c - 1$ . The discretized state is defined as

$$\mathbf{x}(t) := (X(t, \xi_1), X(t, \xi_2), \dots, X(t, \xi_n))^T : [0, t_f] \rightarrow \mathbb{R}^n,$$

and the PDE (6.1) becomes a system of ODEs in  $n$  dimensions:

$$\dot{\mathbf{x}} = \mathbf{x} \circ \mathbf{D}\mathbf{x} + \nu \mathbf{D}^2 \mathbf{x} + \alpha \mathbf{x} \circ e^{\beta \mathbf{x}} + \mathbf{I}_\Omega u,$$

$n$	num. trajectories	training time	value MAE	gradient MRL <sup>2</sup>
10	132	10.1 min	$2.4 \times 10^{-3}$	$1.8 \times 10^{-2}$
20	60	9.2 min	$8.9 \times 10^{-4}$	$2.1 \times 10^{-2}$
30	59	13.3 min	$5.0 \times 10^{-4}$	$2.0 \times 10^{-2}$

Table 3: Validation accuracy of NNs for solving the collocated Burgers’-type optimal control problem (6.3), depending on the state dimension  $n$ . All NNs are trained on an NVIDIA RTX2080Ti GPU.

In the above, the open circle “ $\circ$ ” denotes element-wise multiplication,  $\mathbf{I}_\Omega$  is the discretized indicator function, and  $\mathbf{D}, \mathbf{D}^2 \in \mathbb{R}^{n \times n}$  are the internal parts of the first and second order Chebyshev differentiation matrices, obtained by deleting the first and last rows and columns of the full matrices. This automatically enforces the boundary conditions. Finally, since  $X(t, \xi)$  is collocated at Chebyshev nodes, the inner product appearing in the cost function is conveniently approximated by Clenshaw-Curtis quadrature [31]:

$$\|X(\tau, \xi)\|_{L^2_{(-1,1)}}^2 = \int_{-1}^1 |X(\tau, \xi)|^2 d\xi \approx \mathbf{w}^T \mathbf{x}^2(\tau),$$

where  $\mathbf{w} \in \mathbb{R}^n$  are the internal Clenshaw-Curtis quadrature weights and  $\mathbf{x}^2(t)$  is calculated element-wise, i.e.  $\mathbf{x}^2 = \mathbf{x} \circ \mathbf{x}$ . Now the original optimal control problem (6.2) can be reformulated as an ODE-constrained problem,

$$\begin{cases} \underset{u(\cdot)}{\text{minimize}} & \int_t^{t_f} \frac{1}{2} [\mathbf{w}^T \mathbf{x}^2(\tau) + W_1 u^2(\tau, \mathbf{x})] d\tau + \frac{W_2}{2} \mathbf{w}^T \mathbf{x}^2(t_f), \\ \text{subject to} & \dot{\mathbf{x}} = \mathbf{x} \circ \mathbf{D}\mathbf{x} + \nu \mathbf{D}^2 \mathbf{x} + \alpha \mathbf{x} \circ e^{\beta \mathbf{x}} + \mathbf{I}_\Omega u. \end{cases} \quad (6.3)$$

## 6.1 Learning high-dimensional value functions

The state dimension  $n$  of the optimal control problem (6.3) introduced in the previous section can be adjusted, presenting a good opportunity to test the scalability of our algorithms. For this problem, we learn the value function  $V = V(t, \mathbf{x})$  with time-dependence, rather than just  $V(0, \mathbf{x})$  as in Section 5. Consequently, the resulting controls are time-dependent instead of model predictive. The spatial domain of initial conditions we consider is

$$\mathcal{X}_0 = \{\mathbf{x} \in \mathbb{R}^n \mid -2 \leq x_j \leq 2, j = 1, 2, \dots, n\}.$$

Using the proposed adaptive deep learning framework, we approximate solutions to (6.3) in  $n = 10, 20$ , and 30 dimensions. We focus on demonstrating what is possible using our approach, rather than carrying out a detailed study of its effectiveness under different parameter tunings. In [18] the infinite-horizon version of the problem is solved up to twelve dimensions, but the accuracy of the solution is not readily verifiable. The ability to conveniently measure model accuracy for general high-dimensional problems with *no known analytical solution* is a key advantage of our framework.

For each discretized optimal control problem,  $n = 10, 20$ , and 30, we apply the time-marching strategy to build an initial training data set  $\mathcal{D}_{\text{train}}^1$  from 30 uniformly sampled

initial conditions,  $\mathbf{x}^{(i)} \in \mathcal{X}_0$ ,  $i = 1, 2, \dots, 30$ . For each initial condition  $\mathbf{x}_0^{(i)}$ , the BVP solver outputs an optimal trajectory  $\mathbf{x}^{(i)}(t^{(k)})$ , where  $t^{(k)} \in [0, t_f]$  are collocation points chosen by the solver. Typically this can be a few hundred per initial condition, depending on the state dimension  $n$  and the BVP solver tolerances. As such, we train the NN on a subset of the available data, randomly selected before each round  $r$ . When needed, we solve additional BVPs to expand the data set as described in Section 4.2. We use the same NN architecture as in Section 5, with three hidden layers with 64 neurons each. We manually tune the hyperparameter schedules, e.g.  $\mu = \mu(r)$ , but we omit these details to focus on the outcomes.

In Table 3, we present validation accuracy results for the trained NNs. We include the MAE in predicting the value function and the  $MRL^2$  error in predicting the costate,  $\boldsymbol{\lambda}(t; \mathbf{x}) \approx V_{\mathbf{x}}^{NN}(t, \mathbf{x})$ . Accuracy is measured empirically on independently generated validation data sets comprised of trajectories from 50 randomly selected initial conditions. We find that the trained NNs have good accuracy in both value and costate prediction, even in 30 dimensions.

Table 3 also shows the total number of sample trajectories seen by the NN, including the initial data  $\bar{\mathcal{D}}_{\text{train}}^1$ . It may seem surprising that the number of sample trajectories decreases with the dimension  $n$ . This happens because the BVP solver usually needs more collocation points for larger problems, thus producing more data per trajectory. Consequently, fewer trajectories need to be integrated to fulfill the data set size recommendation (4.8). Similarly, in Section 5 we use data only for  $t = 0$ , so we need thousands of trajectories to fill in the state space and train the NN. This suggests that learning the time dependent value function can be more efficient than a MPC implementation.

Lastly, Table 3 shows the training time for each NN, including time spent generating additional trajectories on the fly but not time spent generating the initial data. Generating the initial data set quickly becomes the most expensive computation as  $n$  increases, but once some data is available, we find that computational effort scales reasonably with the problem dimension. This demonstrates the viability of the proposed method for solving high-dimensional optimal control problems.

## 6.2 Adaptive sampling and fast BVP solutions

In our experience, generating the initial training data set can be the most computationally expensive part of the process, especially as the problem dimension  $n$  increases. Consequently, for difficult high-dimensional problems it may be infeasible to generate a large-enough data set from scratch. This obstacle can be largely overcome by using partially-trained/low-fidelity NNs to aid in further data generation. In this section, we briefly compare the reliability and speed of BVP convergence between our two strategies: time-marching and NN warm start. These experiments demonstrate the importance of NN guesses for high-dimensional data generation.

For each of  $n = 10, 20$ , and  $30$ , we randomly sample a set of 1000 candidate points from the domain  $\mathcal{X}_0$ , from which we pick 100 points with the largest predicted value gradient. The set of initial conditions is fixed for each  $n$ . Next we proceed as in Section 5.2, solving each BVP by time-marching with various  $K$ . Results are summarized in Table 4. We then solve the same BVPs directly over the whole time interval  $t \in [0, 8]$  with NN warm start. These NNs are trained only for a single round on fixed data sets containing 30 trajectories,



$n$	$K$	% BVP convergence	mean integration time
10	4	40%	0.7 s
	6	83%	0.8 s
	10	90%	1.3 s
20	4	46%	3.6 s
	5	86%	4.2 s
	6	99%	4.7 s
30	4	47%	11.3 s
	6	90%	14.6 s
	8	100%	19.1 s

Table 4: Convergence of BVP solutions for (6.3) when using the time-marching trick, depending on the problem dimension,  $n$ , and the number of steps in the sequence  $\{t_k\}_{k=1}^K$ . BVP integration time is measured only on successful attempts.

$n$	$\mu$	gradient $MRL^2$	% BVP convergence	mean integration time
10	0	$1.9 \times 10^0$	96%	0.6 s
	$10^{-1}$	$5.0 \times 10^{-2}$	95%	0.5 s
	$10^1$	$3.5 \times 10^{-2}$	96%	0.6 s
20	0	$8.7 \times 10^0$	63%	2.5 s
	$10^{-1}$	$2.0 \times 10^{-1}$	99%	2.4 s
	$10^1$	$2.7 \times 10^{-2}$	100%	2.3 s
30	0	$6.3 \times 10^0$	89%	7.0 s
	$10^{-1}$	$3.1 \times 10^{-1}$	97%	7.0 s
	$10^1$	$3.8 \times 10^{-2}$	100%	6.8 s

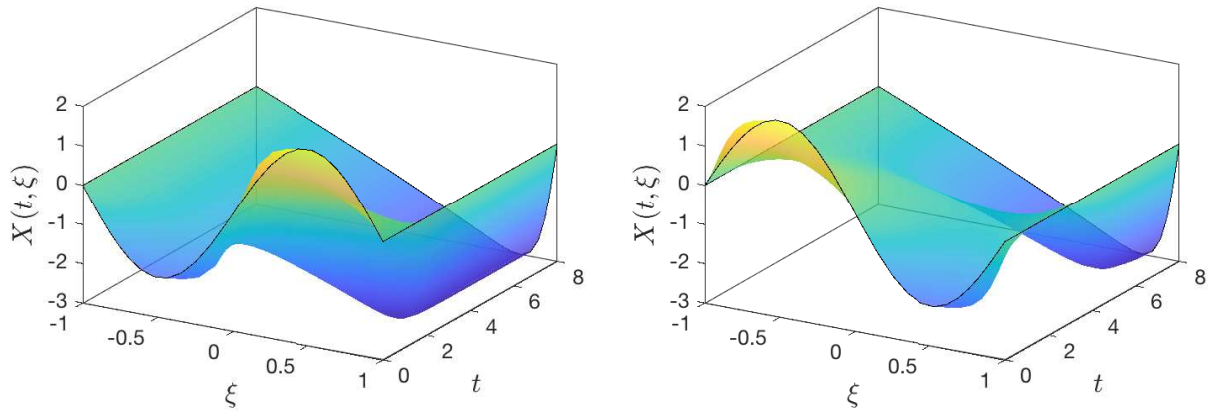
Table 5: Convergence of BVP solutions for (6.3) when using NN warm start with NNs of varying gradient prediction accuracy. BVP integration time is measured only on successful attempts.

but with different gradient weights,  $\mu$ , and thus have varying costate prediction accuracy. Results are given in Table 5.

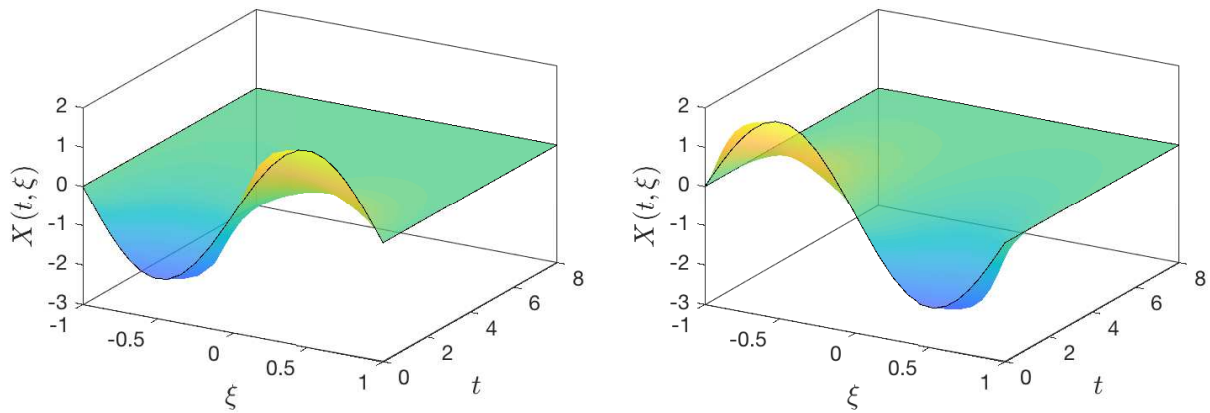
As before, we find that even NNs with relatively large costate prediction error enable consistently convergent BVP solutions. Time-marching also works once the sequence of time steps  $\{t_k\}_{k=1}^K$  is properly tuned, but the speed of this method scales poorly with  $n$ . Now the advantage of utilizing NNs to aid in data generation becomes clear: the average time needed for convergence when using the NN approach is drastically lower than that of the time-marching trick. Because low-fidelity NNs are quick to train, training such a NN and then using it to aid in data generation is the most efficient strategy for building larger data sets.

### 6.3 Closed-loop simulations

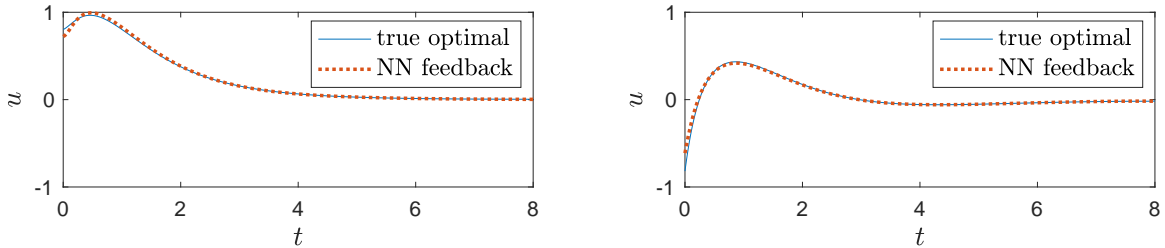
In this section we show that the feedback control output by the trained NN not only stabilizes the high-dimensional system, but that it is close to the true optimal control. The optimal



(a) Uncontrolled dynamics.



(b) NN-controlled dynamics.



(c) Comparison of true optimal control (open-loop BVP solution) and NN control profiles.

Figure 4: Simulations of the collocated Burgers'-type PDE (6.1) in  $n = 30$  dimensions. Left column:  $X(0, \xi) = 2 \sin(\pi\xi)$ . Right column:  $X(0, \xi) = -2 \sin(\pi\xi)$ .

feedback control law can again be calculated with (3.6), from which we obtain

$$u^*(t, \mathbf{x}) = -\frac{1}{W_1} [\mathbf{I}_\Omega]^T V_{\mathbf{x}}(t, \mathbf{x}). \quad (6.4)$$

In Figure 4, we plot the uncontrolled (Figure 4a) and closed-loop controlled dynamics (Figure 4b), starting from two different initial conditions,  $X(0, \xi) = 2 \sin(\pi\xi)$  and  $X(0, \xi) = -2 \sin(\pi\xi)$ , where the dimension of the discretized system is  $n = 30$ . For both of these initial conditions (and almost all others tested), the NN controller successfully stabilizes the

open-loop unstable origin. Further, as shown in Figure 4c, the NN-generated controls are very close to the true optimal controls which are calculated by solving the associated BVPs. Finally, the speed of online control computation is not sensitive to the problem dimension: each evaluation still takes just  $O(10^{-3})$  seconds on both an NVIDIA RTX 2080Ti GPU and a 2012 MacBook Pro.

## 7 Conclusion

In this paper, we have developed a novel machine learning framework for solving HJB equations and synthesizing optimal feedback controls in real-time. Unlike most other state of the art techniques, our method requires no linearization or restrictions on the structure of the dynamics. The causality-free algorithm we use for data generation enables application to high-dimensional systems, as well as validation of model accuracy. We also emphasize that while our method is data-driven, by leveraging the costate data we are able to learn more physically-consistent models and better controls with surprisingly small data sets.

The proposed method is not only a consumer of data, but through adaptive data generation it can also be used build rich data sets with points anywhere in a (semi-global) domain. Thus the value function and control are valid for large ranges of dynamic states, rather than just in the neighborhood of some nominal trajectory. Furthermore, data can be generated near complicated or non-smooth regions of the value function to aid in learning. This in turn allows us to train more accurate NN models, or employ other data-driven methods.

We have demonstrated the possibility for use of the framework in a practical setting by synthesizing nonlinear model predictive feedback controls of a six-dimensional nonlinear rigid body. Scalability of the method is demonstrated by solving HJB equations in up to 30 dimensions using limited data, and empirical validation indicates that the NN models are good approximations of the true value function.

These promising results leave plenty of room for future development. Of special interest are extensions of the framework to solve problems with free final time, state and control constraints, and non-differentiable value functions, which appear ubiquitously in practical applications. Such problems present substantial challenges for both data generation and neural network modeling. Overcoming these obstacles would open the door to solving many important and difficult optimal control problems.

## References

- [1] M. ABADI, A. AGARWAL, P. BARHAM, ET AL., *TensorFlow: Large-scale machine learning on heterogeneous systems*. <http://www.tensorflow.org/>, 2015–.
- [2] E. AL'BREKHT, *On the optimal stabilization of nonlinear systems*, J. Appl. Math. Mech., 25(5) (1961), pp. 1254–1266.
- [3] O. BOKANOWSKI, J. GARCKE, M. GRIEBEL, AND I. KLONPMAKER, *An adaptive sparse grid semi-Lagrangian scheme for first order Hamilton-Jacobi Bellman equations*, J. Sci. Comput., 55 (2013), pp. 575–605.

- [4] L. BOTTOU, F. E. CURTIS, AND J. NOCEDAL, *Optimization methods for large-scale machine learning*, SIAM Rev., 60 (2018), pp. 223–311.
- [5] A. BRESSAN AND B. PICCOLI, *Introduction to the Mathematical Theory of Control*, American Institute of Mathematical Sciences, 2007.
- [6] R. H. BYRD, G. M. CHIN, J. NOCEDAL, AND Y. WU, *Sample size selection in optimization methods for machine learning*, Math. Program., 134 (2012), pp. 127–155.
- [7] R. H. BYRD, P. LU, J. NOCEDAL, AND C. ZHU, *A limited memory algorithm for bound constrained optimization*, SIAM J. Sci. Comput., 16 (1995), pp. 1190–1208.
- [8] S. CACACE, E. CRISTIANI, M. FALCONE, AND A. PICARELLI, *A patchy dynamic programming scheme for a class of Hamilton–Jacobi–Bellman equations*, SIAM J. Sci. Comput., 34(5) (2012), pp. A2625–A2649.
- [9] Y. T. CHOW, J. DARBON, S. OSHER, AND W. YIN, *Algorithm for overcoming the curse of dimensionality for state-dependent Hamilton–Jacobi equations*, J. Comput. Phys., 387 (2019), pp. 376–409.
- [10] J. DARBON AND S. OSHER, *Algorithms for overcoming the curse of dimensionality for certain Hamilton–Jacobi equations arising in control theory and elsewhere*, arXiv:1605.01799, (2016).
- [11] J. DIEBEL, *Representing attitude: Euler angles, unit quaternions, and rotation vectors*. [https://www.astro.rug.nl/software/kapteyn-beta/\\_downloads/attitude.pdf](https://www.astro.rug.nl/software/kapteyn-beta/_downloads/attitude.pdf), 2006.
- [12] M. FALCONE AND R. FERRETTI, *Semi-Lagrangian Approximation Schemes for Linear and Hamilton–Jacobi Equations*, Society for Industrial and Applied Mathematics, 2013.
- [13] J. HAN, A. JENTZEN, AND W. E, *Solving high-dimensional partial differential equations using deep learning*, Proceedings of the National Academy of Sciences, 115 (2018), pp. 8505–8510.
- [14] R. HARTL, S. SETHI, AND R. VICKSON, *A survey of the maximum principles for optimal control problems with state constraints*, SIAM Rev., 37 (1995), pp. 181–218.
- [15] D. IZZO, E. ÖZTÜRK, AND M. MÄRTENS, *Interplanetary transfers via deep representations of the optimal policy and/or of the value function*, arXiv:1904.08809, (2019).
- [16] F. JIANG, G. CHOU, M. CHEN, AND C. J. TOMLIN, *Using neural networks to compute approximate and guaranteed feasible Hamilton–Jacobi–Bellman PDE solutions*, arXiv:1611.03158, (2016).
- [17] E. JONES, T. OLIPHANT, P. PETERSON, ET AL., *SciPy: Open source scientific tools for Python*. <http://www.scipy.org/>, 2001–.
- [18] D. KALISE AND K. KUNISCH, *Polynomial approximation of high-dimensional Hamilton–Jacobi–Bellman equations and applications to feedback control of semilinear parabolic PDEs*, SIAM J. Sci. Comput., 40 (2018), pp. A629–A652.

- [19] W. KANG, P. DE, AND A. ISIDORI, *Flight control in a windshear via nonlinear  $h_\infty$  methods*, in Proceedings of the 31st IEEE Conference on Decision and Control, 1992, pp. 1135–1142.
- [20] W. KANG AND L. C. WILCOX, *A causality free computational method for HJB equations with application to rigid body satellites*, in AIAA Guidance, Navigations, and Control Conference, 2015.
- [21] W. KANG AND L. C. WILCOX, *Mitigating the curse of dimensionality: Sparse grid characteristics method for optimal feedback control and HJB equations*, Comput. Optim. Appl., 68 (2017), pp. 289–315.
- [22] W. KANG AND L. C. WILCOX, *Solving 1D conservation laws using Pontryagin’s minimum principle*, J. Sci. Comput., 71(1) (2017), pp. 144–165.
- [23] J. KIERZENKA AND L. F. SHAMPINE, *A BVP solver based on residual control and the MATLAB PSE*, ACM Trans. Math. Softw., 27 (2001), pp. 299–316.
- [24] D. LIBERZON, *Calculus of Variations and Optimal Control Theory: A Concise Introduction*, Princeton University Press, Princeton, NJ, USA, 2011.
- [25] D. LUKES, *Optimal regulation of nonlinear dynamical systems*, SIAM J. Control, 7(1) (1969), pp. 75–100.
- [26] C. NAVASCA AND A. J. KRENER, *Patchy solutions of Hamilton-Jacobi-Bellman partial differential equations*, in Modeling, Estimation and Control, A. Chiuso, S. Pinzoni, and A. Ferrante, eds., vol. 364 of Lecture Notes in Control and Information Sciences, Springer-Verlag Berlin Heidelberg, 2007, pp. 251–270.
- [27] M. RAISSI, *Forward-backward stochastic neural networks: deep learning of high-dimensional partial differential equations*, arXiv:1804.07010, (2018).
- [28] M. RAISSI, P. PERDIKARIS, AND G. KARNIADAKIS, *Physics-informed neural networks: A deep learning framework for solving forward and inverse problems involving nonlinear partial differential equations*, J. Comput. Phys., 378 (2018).
- [29] J. SIRIGNANO AND K. SPILIOPOULOS, *DGM: A deep learning algorithm for solving partial differential equations*, J. Comput. Phys., 375 (2018), pp. 1339 – 1364.
- [30] Y. TASSA AND T. EREZ, *Least squares solutions of the HJB equation with neural network value-function approximators*, IEEE Trans. Neural Netw., 18 (2007), pp. 1031–1041.
- [31] L. N. TREFETHEN, *Spectral Methods in MATLAB*, Society for Industrial and Applied Mathematics, 2000.
- [32] I. YEGOROV AND P. M. DOWER, *Perspectives on characteristics based curse-of-dimensionality-free numerical approaches for solving Hamilton-Jacobi equations*, Appl. Math. Optim., (2018).